HHS Public Access

Author manuscript

Circ Arrhythm Electrophysiol. Author manuscript; available in PMC 2016 October 01.

Published in final edited form as:

Circ Arrhythm Electrophysiol. 2015 October ; 8(5): 1228–1239. doi:10.1161/CIRCEP.115.003155.

Direct Measurement of Cardiac Na^+ Channel Conformations Reveals Molecular Pathologiesof Inherited Mutations

Zoltan Varga, PhD[1,2], **Wandi Zhu, BS**[1], **Angela R. Schubert, BS**[1], **Jennifer L. Pardieck, BS**[1], **Arie Krumholz, PhD**[1], **Eric J. Hsu, BS**[1], **Mark A. Zaydman, BS**[1], **Jianmin Cui, PhD**[1], and **Jonathan R. Silva, PhD**[1]

[1]Department of Biomedical Engineering, Washington University in St. Louis, St. Louis, MO

[2]MTA-DE-NAP B Ion Channel Structure-Function Research Group, RCMM, University of Debrecen, Debrecen, Hungary

Abstract

Background—Dysregulation of voltage-gated cardiac Na^+ channels ($Na_V1.5$) by inherited mutations, disease-linked remodeling, and drugs causes arrhythmias. The molecular mechanisms whereby the $Na_V1.5$ voltage-sensing domains (VSDs) are perturbed to pathologically or therapeutically modulate Na^+ current (I_{Na}) have not been specified. Our aim was to correlate I_{Na} kinetics with conformational changes within the four (DI-DIV) VSDs to define molecular mechanisms of $Na_V1.5$ modulation.

Method and Results—Four $Na_V1.5$ constructs were created to track the voltage-dependent kinetics of conformational changes within each VSD, using voltage-clamp fluorometry (VCF). Each VSD displayed unique kinetics, consistent with distinct roles in determining I_{Na}. In particular, DIII-VSD deactivation kinetics were modulated by depolarizing pulses with durations in the intermediate time domain that modulates late I_{Na}. We then used the DII-VSD construct to probe the molecular pathology of two Brugada Syndrome (BrS) mutations (A735V and G752R). A735V shifted DII-VSD voltage-dependence to depolarized potentials, while G752R significantly slowed DII-VSD kinetics. Both mutations slowed I_{Na} activation, even though DII-VSD activation occurred at higher potentials (A735V) or at later times (G752R) than ionic current activation, indicating that the DII-VSD allosterically regulates the rate ofI_{Na} activation and myocyte excitability.

Conclusions—Our results reveal novel mechanisms whereby the $Na_V1.5$ VSDs regulate its activation and inactivation. The ability to distinguish distinct molecular mechanisms of proximal BrS mutations demonstrates the potential of these methods to reveal how inherited mutations, post-translational modifications and anti-arrhythmic drugs alter $Na_V1.5$ at the molecular level.

Keywords

sodium channels; Brugada syndrome; ion channel

Correspondence: Jonathan R. Silva, PhD, Washington University in St. Louis, Campus Box 1097, 1 Brookings Dr., St. Louis, MO 63130, Tel: 314-935-8837, Fax: 314-935-7448, jonsilva@wustl.edu.

Conflict of Interest Disclosures: None.

Introduction

Atrial and ventricular action potentials (AP) are initiated by a large membrane-depolarizing Na^+ flux through the cardiac voltage-gated Na^+ channel, $Na_V1.5$. In large animals and humans, persistent $Na_V1.5$ current is also a significant regulator of AP duration. Because of its central role in determining the AP, molecular-level interactions that perturb $Na_V1.5$ channel function have a significant impact on the ability of the myocardium to initiate and sustain arrhythmias. Mutations to $Na_V1.5$ are known to cause Long QT Syndrome Type 3 (LQT3), Brugada Syndrome (BrS), Sick Sinus Syndrome, Atrial Fibrillation and Familial Heart Block[1, 2]. Further, class I small molecule anti-arrhythmics target the $Na_V1.5$ pore with the aim of diminishing Na^+ current to prevent arrhythmia[3]. To date, characterization of $Na_V1.5$ mutation pathology and drug interactions hasprimarily relied on measuring the ionic current response to elaborately designed voltage-pulse protocols. Here, we develop novel $Na_V1.5$ constructs to augment these protocols by monitoring changes in conformation with fluorescence labeling, at the same time that we observe the ionic current, with voltage-clamp fluorometry (VCF). By applying VCF to observe channels that carry inherited mutations, we expect to improve phenotypic precision by characterizing the molecular pathology of the disease.

The $Na_V1.5$ α-subunit, encoded by *SCN5A*, is composed of four homologous domains (DI-DIV), each with six transmembrane-spanning segments (S1-S6). Within DI-DIV, S1-S4 form the voltage-sensing domains (VSD), which respond to changes in membrane potential (V_m) to cause $Na_V1.5$ gating. The $Na_V1.5$ pore is formed by the S5-S6 segments. A hydrophobic triplet (IFM) located in the intracellular DIII/DIV linker is required for inactivation[4], and its action is modulated by the C-terminus[5].

Previously, VCF was used to relate skeletal muscle Na^+ channel, $Na_V1.4$, VSD conformations to channel activation and inactivation[6-10] and to probe the domain-specific interactions of toxins[11-13] and local anesthetics[14, 15].

In this study, we present four novel constructs that report on the distinctive VSD conformations of $Na_V1.5$for the purpose of assessing molecular mechanisms of $Na_V1.5$-linked pathologies and therapies. To demonstrate the potential of the method, we probe the molecular phenotype of two proximal BrS1 mutations, A735V and G752R, which are both located on the DII-VSD. The ECG phenotypes of patients with each mutation differ. Patients with A735V present with S-T segment elevation in leads V1-V3[16], while those with G752R show S-T segment elevation[17] in addition to a prominent J wave in leads II, III, and aVF[18]. We hypothesized that in addition to ECG differences, there may also exist fundamentally different molecular pathologies, despite the proximity of the mutations.

Materials and Methods

Voltage clamp fluorometry

cRNAs for human $Na_V1.5$ α- and β_1-subunits were injected into *Xenopuslaevis* oocytes for cut-open oocyte recordings[19, 20] at 19°C. The internal solution was (mmol/L): 105 NMG-Mes, 10 Na-Mes, 20 HEPES, and 2 EGTA, pH 7.4, and the external solution was composed

of (mM): 25 NMG-Mes, 90 Na-Mes, 20 HEPES, and 2 Ca-Mes_2, pH 7.4. For gating currents, 10 μM TTX was used, and Na-Mes was replaced by NMG-Mes. For fluorescence recordings, oocytes were labeled with 10 μmol/L methanethiosulfonate-carboxytetramethylrhodamine (MTS-TAMRA). Data was collected on a custom rig (see *Supplemental Methods*). Animal procedures were performed according to institutional guidelines.

Data analysis

For photobleaching correction, baseline fluorescence recorded over time without voltage pulsing was subtracted from traces recorded during the application of the voltage protocol. Fluorescence magnitude is expressed as $\Delta F/F_0$, ΔF is the signal amplitude change and F_0 is baseline fluorescence.

Steady-state voltage-dependence was quantified by Boltzmann-function fitting: $y=1/(1+\exp[(V-V_{1/2})/k)]$. $t_{10\text{-}90\%}$ for current activation is the duration between 10 and 90% of the ionic current peak. For fluorescence signals, $t_{10\text{-}90\%C}$ was calculated from the time constants of single exponential fits τ.

Statistical comparisons were done using paired or independent-sample t-tests or one-way ANOVA with post-hoc tests for pairwise comparison. $p<0.05$ was considered significant. The ± symbols in the text and error bars in the figures represent the 95% confidence interval(95CI) with number of trials (n) in parentheses.

Results

Our first aim was to create four $Na_V1.5$ constructs to track conformational changes within each of the $Na_V1.5$ channel VSDs. Initial attempts to record fluorescence signals were unsuccessful due to insufficient expression of human $Na_V1.5$, which is significantly reduced compared to rat $Na_V1.4$, the isoform used to acquire most existing Na^+ channel VCF data. Examination of differences between the two channels revealed that $Na_V1.5$ contains an ubiquitination motif that enhances the channel recycling rate and reduces the number of channels in the membrane[21]; this motif is not found in $Na_V1.4$. Ablation of the ubiquitination site by the Y1977A mutation and co-injection with β_1-subunit RNA resulted in sufficient $Na_V1.5$ expression for the detection of useful fluorescence signals. We also introduced C373Y, increasingtetrodotoxin[22] (TTX) sensitivity and allowing ionic current blockade for the measurement of gating currents. This mutation also removes an externally accessible cysteine, preventing non-specific labeling.

Two protocols were performed to compare our new construct to wild type. We first quantified the conductance-voltage (G-V) relationship, found by measuring peak current after a series of depolarizing pulses and dividing by driving force. The second protocol measured the voltage-dependence of steady state inactivation (SSI); peak current was measured during a short test pulse to -20 mV that followed 200-ms inactivation-inducing pulses to varying potentials. The voltage-dependence of the G-V and SSI curves were not substantially affected by these mutations (Fig. 1, p=0.951 and 0.069, respectively). For fluorescence tracking, cysteine mutations (specified below) in the individual domains were

introduced in this Y1977A-C373Y mutant, which we named WT-LFS (Large Fluorescence Signal). The mutants produced for VSD-tracking in this background will be accordingly referred to as DI-LFS, DII-LFS, DIII-LFS, and DIV-LFS. Cysteines were introduced at several positions within each VSD, but most of these did not produce useful signals. We were fortunate to find a single useful site for each domain.

To track the conformation of the DI-VSD, we tested ten positions from L212 to T220 and R222. V215C (DI-LFS) was the only mutant to express well and produce a usable fluorescence signal (Fig 2). The $Na_V1.5$ VSDs play an essential role in determining gating, and we expected the TAMRA-MTS labeling in conjunction with the introduced cysteine to affect gating to some extent. We observed a negative shift ($\Delta V_{1/2}$=-16.8 mV) in the G-V and a slight positive shift ($\Delta V_{1/2}$=+8 mV) in the SSI curves compared to the background WT-LFS construct, implying that the labeled V215C channel opens at more negative potentials and inactivates at more positive potentials than WT-LFS. Comparing labeled and unlabeled DI-LFS showed that the G-V shift is a consequence of adding the TAMRA-MTS label (Figure S1). We also used gating currents to assess whether charge movement across the transmembrane electric field was affected by labeling (Fig. S2). If the probe significantly affected charge transfer, we would expect to observe a change in the voltage-dependence of the gating current integral, the gating charge. For the four constructs, the charge-voltage (Q-V) relationship was shifted over a range of 5 to 11 mV in comparison to WT-LFS (Fig. S1 and Table 1), suggesting that charge displacement was modestly affected by cysteine-conjugated fluorophore replacement of the WT residue.

Simultaneously recording changes in fluorescence magnitude during these protocols allowed us to correlate DI-VSD conformations to channel gating. We refer to the fluorescence that was recorded during the G-V protocol as the fluorescence-voltage relationship (F-V curve) and the fluorescence from the SSI protocols as the SSIF-V curve. The F-V curves reflect the voltage-dependence of the conformations in the DI-VSD that are reported by TAMRA. For the DI-VSD, the midpoint of the F-V curve was 27.2 mV negative of the G-V curve, indicating that DI-VSD movement occurs at much more negative potentials than pore opening. On the contrary, the SSI and SSI F-V curves had very similar midpoints, showing that inactivation and DI-VSD movement occur in the same voltage range. However, in contrast to DIV (see below), the DI-VSD SSI F-V and SSI slopes differed substantially (k=-15.4(5) vs -6.4 mV(8), respectively, $p<0.001$), suggesting that the two events are not tightly coupled.

The fluorescence kinetics recorded during the F-V curve reflect the voltage-dependent rates of VSD activation and deactivation. Since current and VSD activation kinetics are described by different functions, we measured the time between 10% and 90 % of the peak current and calculated $t_{10\text{-}90\%C}$ for fluorescence(see Methods). DI-VS Drise-time was slower($t_{10\text{-}90\%C}$=0.82±0.23ms at +30 mV) than ionic current activation ($t_{10\text{-}90\%}$=0.24±0.04ms), but the events overlapped due to the sigmoidal delay in ionic current activation (Fig. S3). At elevated potentials (>+20 mV) a slow component in the DI-VSD fluorescence signal became apparent with an opposite sign relative to the original deflection. While significant numbers of channels will not make this slow transitionto a new state during a single AP, channels may accumulate in this state at rapid heart rates.

Since fast inactivation is known to hinder the recovery of the gating charges upon repolarization (immobilization), we performed experiments to measure the deactivation rate of the DI-VSD after depolarizing pulses of varying length, which inactivated the channels to different extents. The deactivation kinetics measured at -120 mV did not change as a function of pulse duration($t_{10\text{-}90\%C}$=0.99±0.22ms after a 2 ms pulse and 0.99±0.13ms after a 200 ms pulse, (4), p=0.948). This result suggests that DI-VSD deactivation is not influenced by $Na_V1.5$ open-state inactivation, which had not occurred during the 2 ms pulse and is nearly complete after 200 ms.

We tracked the DII-VSD with S805C (DII-LFS), which yielded large and robust signals. The voltage-dependent steady-state parameters (G-V and SSI curves) were minimally affected in comparison to WT-LFS; there was no shift in the G-V curve and a +7.4 mV shift in the SSI curve (Fig. 3). Measurement of the F-V revealed that it was 12.5 mV negative of the G-V curve, showing that the DII-VSD starts to move prior to activation; however, it reaches saturation at higher potentials than the conductance due to its shallower slope, which indicates that the two events are not tightly coupled. Comparing the SSI and SSI-FV curves shows that inactivation occurs at more negative potentials than DII-VSD activation($V_{½}$=-79.2 and -52.2 mV, respectively), and that the inactivation slope is much steeper than DII-VSD activation(k=-6.5and-17.5 mV, respectively, (7,6), p<0.001). Thus, at holding potentials which completely abolish the conductance by inactivation (V>-50 mV), the DII-VSD is still far from having completed its motion, likely precluding it from participating in closed-state inactivation. The DI-VSD and DII-VSDs activate at similar rates ($t_{10\text{-}90\%C}$=0.98±0.19msat +30 mV, (5) p=0.332), and, when superimposed on the ionic current, DII-VSD activation precedes ionic current activation (Fig. S3). As for DI, the DII-VSD deactivation kinetics are not substantially affected by the length of the depolarizing pulse ($t_{10\text{-}90\%C}$=0.86±0.29ms after 2 ms and 0.99±0.13ms after 200 ms, (4), p=0.171).

Conformations in the DIII-VSD were tracked with M1296C (DIII-LFS), which was the only construct to produce a signal out of I1299C, K1300C, and S1301C. The DIII construct had G-V and SSI curves nearly identical to those of DII, but relative to the DII-VSD, the F-V and SSI F-V curves were dramatically shifted by -54.6 and -70.3 mV, respectively (Fig. 4). Comparison to the G-V and SSI curves shows that DIII-VSD activation precedes pore opening by a large voltage margin during activation, and similarly, during inactivation, most of the VSD movement is completed before any noticeable drop in the conductance due to inactivation. Activation kinetics of the DIII-VSD were similar to those of DI and DII ($t_{10\text{-}90\%C}$ = 0.81±0.25ms at +30 mV, (5), p=0.332), although deactivation was >10× slower. Furthermore, in contrast to DI and DII, the deactivation kinetics of the DIII-VSD were significantly slowed when the duration of depolarizing pulse was increased ($t_{10\text{-}90\%C}$ = 12.85±2.37 ms after a 2 mspulse and 18.58±1.58 after 200 ms, (6), p=0.009). The markedly slowed deactivation of the DIII-VSD following long depolarizations indicates that its return could be inhibited by entry of the channel into the deeper inactivated states that occur after longer depolarizations, which stabilize it in the activated conformation.

Finally, to track the DIV-VSD, we introduced S1618C (DIV-LFS) and L1621C (no signal). The unlabeled DIV-LFS construct displays a non-saturating SSI curve that is corrected by fluorophore conjugation. Recording of the unlabeled construct with a reducing agent

confirmed that this phenomenon was due to disulphide bond formation in the absence of the fluorophore (Figure S1). Both the G-V and SSI curves of the DIV-VSD construct were shifted relative to WT-LFS by +5.3 and +12.4 mV, respectively (Fig. 5). Comparison of the fluorescence and ionic current shows that the midpoint of the F-V curve was 32.2 mV more negative than that of the G-V, while the SSI and SSI F-V curves overlapped, further supporting strong correlation between DIV-VSD activation and closed-state inactivation that is primarily measured by the SSI curve. In addition, slowing of fast inactivation caused by the introduction of the cysteine mutation is also readily apparent in the ionic current recordings. In comparison to the other three domains, the DIV fluorescence signal activated much more slowly ($t_{10\text{-}90\%C}$=1.91±0.44ms at +30 mV, (7), p<0.001). Deactivation kinetics were significantly slower than those of the DI and DII, but 2-3 times faster than that of DIII. Surprisingly, DIV-VSD deactivation did not slow with increasing pulse duration ($t_{10\text{-}90\%C}$=5.71±4.04ms after a 2 ms pulse and 6.63±3.91ms after 200 ms, (4), p=0.411). Given the prominent role of DIV in inactivation, the lack of slowing in DIV-VSD recovery with longer pulses is highly unexpected and is in clear contrast with $Na_V1.4$ results[8], suggesting different interactions between the DIII- and DIV-VSDs and inactivation.

Our next aim was to assess the molecular pathology of two proximal DII-VSD BrS mutations, A735V and G752R (Fig. 6). We introduced each into the DII-LFS construct. The F-V and SSI F-V curves of A735V were dramatically positive-shifted relative to DII-LFS (by+49.1 mV and +58.5 mV, respectively) and also relative to the G-V and SSI curves of the channel itself (by +19.5 mV and +89.1 mV, respectively). In addition, the voltage-sensitivity of the DII-VSD was severely reduced; both had very shallow slope factors (35.4 mV and -39.5 mV, respectively). DII-VSD activation kinetics were also slightly slowed by the mutation at +40 mV based on the $t_{10\text{-}90\%C}$ values (DII-LFS: 0.99±0.19ms (8), DII-LFS-A735V: 1.49±0.36ms, (5), p=0.005), but even more strikingly, the DII-VSD activation rate of the mutant lost its voltage-dependence (1.45±0.42ms at -20 mV and 1.49±0.36ms at +40 mV(5), p=0.850) as opposed to DII-LFS (1.42±0.19ms at -20 mV and 0.99±0.19ms at +40 mV (8), p=0.002). To the contrary, ionic current activation of the mutant conserved its voltage-dependence, but was slower than DII-LF Sat potentials <10 mV ($t_{10\text{-}90\%}$=1.48±0.17ms (5) vs 0.71±0.47 ms (3), respectively, at -20 mV, p=0.002). Despite the severely right-shifted F-V of A735V, the mutant Q-V ($V_{1/2}$= -75.6 ±8.3 mV (5)) was not significantly different from that of DII-LFS (-80.0 ± 7.6 mV (4), p=0.241) or WT-LFS (-69.1 ± 4.2 mV (7), p=0.058).

In contrast, G752R caused minor F-V and SSI F-V shifts (by +1.0 mV and -9.8 mV, respectively, compared to DII-LFS) and displayed similar slope factors, but resulted in a severe slowing of the DII-VSD activation. In response to a depolarizing step, the rate of DII-VSD activation was about 7-fold slower in the mutant than in the DII-LFS channel ($t_{10\text{-}90\%C}$=0.99±0.19 ms (8) and 6.96±1.21ms (8) at +40 mV, respectively, p<0.001). The Q-V curve was right-shifted by ∼20 mV with respect to DII-LFS. However, extending the interval over which charge was integrated from 10 to 20 ms, to account for G752R-induced slowing, shifted the curve leftward and closer to DII-LFS. Significant slowing of activation kinetics was also observed in the ionic current of G752R. In the -40 to +30 mV voltage range, the activation rate was 1.7 to 2.9 times slower than that of the DII-LFS as measured

by the $t_{10\text{-}90\%}$ times (1.51±0.15 ms (7) and 0.71±0.47 ms (3), respectively, at -20 mV, $p<0.001$; Fig S4).

To ensure that the mechanisms we observed in oocytes are still operative across cell lines, we expressed both mutants in HEK293T cells. A comparison (Fig. S5) shows that as in oocytes, current activation measured by the $t_{10\text{-}90\%}$ was slowed in both BrS mutants compared to DII-LFS (at -20 mV, DII-LFS: 0.27±0.09 ms (4), A735V: 0.81±0.32 ms (5), G752R: 0.66±0.07 ms (4); $p=0.002$).

Discussion

Our results represent the first measurements of human $Na_V1.5$ VSD conformations and show that each VSD has unique kinetics, consistent with specific gating roles. Specifically, the four VSDs activate at very different membrane potentials that span a range >50 mV. DIII activates at the most hyperpolarized potentials ($V_{1/2}$=-106.0 mV), followed by DI(-83.9 mV), DIV(-66.8), and finally DII(-51.4), all negative of the G-V curve that characterizes current activation ($V_{1/2}$=-39.9 mV for WT-LFS). Further, all four VSDs have a $t_{10\text{-}90}$ rise time that is slower than ionic current activation, which is to be expected if ionic current activation is due to the combined motions of several VSDs that can be modeled as a cubed gate (*e.g.*,m^3 in Hodgkin-Huxley type models), allowing for a more rapid activation after a delay.

While our results support the hypothesis of concerted action of several VSDs in activating Na_V channels, our mutation results contrast with classical models that require tight coupling of the "gates" to pore opening. Comparing DII-VSD activation voltage-dependence in A735V to its G-V relationship (Fig. 6A) reveals that the channel fully opens at 0 mV, even though the DII-VSD is not fully activated even at +80 mV. This phenomenon is observed in DII-LFS as well, indicating that this property is intrinsic to NaV1.5, but the effect is greatly enhanced in A735V. Thus, DII-VSD activation facilitates channel opening through an allosteric mechanism where lack of VSD-activation simply slows activation, but does not prevent it. This mechanism may be evolutionarily beneficial, because it allows for moderate alteration of VSD kinetics by mutations without preventing Na^+ channel activation and myocyte excitability.

Correlation of VSD-activation with inactivation can be assessed by comparing the SSI and SSI-FV curves and pulse duration protocols. The SSI protocols show that the DII-VSD is least likely to participate in inactivation: At potentials when the channel is completely blocked by inactivation, the DII-VSD has yet to significantly activate (Fig. 3). In contrast, the close overlap of the SSI and DIV SSI F-V curves supports the notion that the closed-state inactivation reported by this protocol is tightly coupled to DIV-VSD movement. Finally, the pulse duration protocol may reveal VSD interaction with deeper inactivation states that occur at depolarized potentials, which are likely to modulate the late Na^+ current.

The origin of ΔF

Our detected changes in TAMRA fluorescence emission are likely due to photo-induced electron transfer, which is a quenching non-radiative electron transfer between two

molecules that are within 10 Å, in close van der Waals contact[23]. Many different residues may quench the fluorophore, which implies that our fluorescence signal is highly dependent on the surrounding residues that interact with the fluorophore as it moves. This dependence introduces the possibility that the fluorescence changes we observe do not necessarily reflect the movement of the charged S4 segments across the membrane.

Our Q-V curves that are calculated from gating currents directly quantify charge transfer within all four domains across the membrane field. Thus, we expect that if we are tracking charge transfer, then the valence-weighted average midpoint of the F-V curves will match the Q-V curves(Figure 7, Table 1)[6]. The WT-LFS Q-V is accurately reconstructed by the valence-weighted F-V curves (Figure 7A). Moreover the confounding left-shift in the A735V Q-V relative to G752R is also predicted by this analysis (Figure 7B), and results from much less charge being assigned to the DII F-V due to its reduced slope, which lessens its right-shifting contribution. With the G752R construct, we observe less charge transferred at some of the lower potentials. This slight difference is likely due to the substantial slowing of charge movement at these potentials, which sharply reduces the gating current and precludes its detection. Alternatively, G752R may be slowing activation of the other three domains, causing a right-shifted Q-V. Previous work in $Na_V1.4$ shows that a DII-VSD activation shift modestly affects the activation of the DI, DIII, and DIV VSDs[25]. Future efforts to probe $Na_V1.5$ cooperativity will be needed to test whether this the case for A735V and G752R.

A simple two-state model of the VSD would predict that the SSI-FV is simply a mirror image of the F-V and that they should cross at 0.5. This is the case for the DI and DII VSDs, but not for the DIII- and DIV-VSDs, which showed a lower crossing. Since the SSI-FV uses a 200 ms pulse, whereas the F-V is measured after several ms, the difference is likely due to multiple activated or resting states of the VSD. This is not surprising, as multiple DIII-VSD resting states have been posited to model lidocaine interaction and we also infer multiple states from the pulse duration protocol. For the DIV-VSD this crossing was in the range of experimental variability, but may be linked to DIV-VSD interaction with inactivation.

Comparison to Previous Results

VCF has been used to study $Na_V1.4$, and many of the results have been extrapolated across the super-family of Na_V channels. While we observe many similarities, there are several distinct $Na_V1.5$ features. In $rNa_V1.4$, the VSD activation midpoints all fell within a 20 mV range. In contrast, midpoints of the F-V curves for $hNa_V1.5$ spanned a range of about 50 mV. In particular, DIII was activated at very hyperpolarized potentials, and DII activation was substantially depolarized relative to the Q-V (by 30 mV). For the DII-VSD, this depolarizing shift may be due to loose coupling between the DII-VSD and channel activation, which was not observed in $Na_V1.4$.

Further differences are seen when comparing the connection between inactivation and VSD activation. Classical studies of Na_V channel gating charge movement found that, following prolonged depolarization, a fraction of the gating charge is “immobilized”: that is, it returns with much slower kinetics upon repolarization than the majority of the charge[26]. In human $Na_V1.4$, this immobilized fraction was associated with DIII and DIV[8]. Consistently,

hNa$_V$1.5DI- and DII-VSD deactivation was independent of the length of the depolarizing pulse. Conversely, return of the hNa$_V$1.5 DIII-VSD was significantly slowed by long depolarizations, while the DIV-VSD deactivation rate was unaffected, in clear contrast to Na$_V$1.4. However, this observation is in agreement with previous reports showing that charge immobilization of the Na$_V$1.5 DIV-VSD is independent of inactivation, and that the inactivation particle can only modulate gating charge recovery of DIII, but not DIV[27]. Thus our data reconciles these two previously discrepant results by showing that the hNa$_V$1.5 VSDs interact with inactivation uniquely.

Many have previously probed the functional contributions of each VSD to Na$_V$ 1.5 gating, and our data shows the timing of these contributions. For example, outward stabilization of the DI-S4 strongly reduced peak Na$_V$1.5 current (45%) without affecting rapid channel kinetics[28]. In our data, we observed a slow DI-VSD transition at elevated potentials that may be linked to this peak reduction through slow inactivation (Figure 2). In contrast, DII-VSD outward stabilization does affect rapid gating kinetics, shifting the G-V leftward along with SSI[28]. Our results show that this DII-VSD regulation of channel activation is through an allosteric connection, which facilitates channel opening when the DII-VSD is activated. Similar work has also probed the consequences of DIII and DIV-VSD outward stabilization[29], both of which alter channel availability without affecting activation. While the link between the four VSDs and inactivation is consistent with our results, it remains to be seen whether a slowing of DI, DIII or DIV may also affect channel activation as observed in DII.

Relevance

For the inherited BrS1 mutations, A735V and G752R, we observed two very different molecular pathologies (Fig 6). A735V clearly shifts the voltage dependence, while at positive potentials DII-VSD activation kinetics are nearly as rapid as WT. In contrast, DII-VSD voltage-dependence is preserved with G752R, but it arrives at its steady state much more slowly. For both mutants, the consequence for the ionic current is slower activation. Thus, our results show that dramatically different molecular pathologies can give rise to very similar ionic current phenotypes. Still, molecular-level differences are likely to have significant consequences for the interaction of the channel with anti-arrhythmic therapies.

From a theoretical perspective, the non-canonical Na$_V$1.5 activation mechanism revealed by the G752R and A735V mutations suggests a very specific Markov state diagram where opening is possible from closed states where the VSDs are not yet activated. Recent work on L-type Ca^{2+} channels revealed that this type of allosteric model was best suited to describe its data. Given the recent attention to similarities between Ca^{2+} and Na^{+} channels it would not be surprising if a similar model would be more suitable for describing Na$_V$1.5 gating. We expect that future work probing the contribution of each VSD to channel gating will be immensely useful for informing these widely used models.

Future Directions

As demonstrated by our ability to observe the molecular pathology of two BrS1 mutations, we expect that we will be able to better understand mechanisms whereby some of the

>150$Na_V1.5$ inherited mutations cause disease. In addition, $Na_V1.5$ is known to interact with many accessory proteins, and it is tightly controlled by post-translational modification. By observing how these modulatory proteins and modifications affect the VSDs, we expect to unravel molecular mechanisms whereby the cell regulates $hNa_V1.5$ gating to modulate cardiac myocyte excitability.

Supplementary Material

Refer to Web version on PubMed Central for supplementary material.

Acknowledgments

We thank Jennifer NA Silva, MD and James Ballard for many helpful discussions and advice.

Funding Sources: Burroughs Wellcome Fund Career Award at the Scientific Interface 1010299 (J.R.S.) and NIH training grant T32-HL007275 (J.R.S), NIH Grants R01-HL70393 and R01-NS060706 (J.C.), American Heart Association fellowship 11PRE5720009 and NIH T32-HL007873 (M.A.Z.), R01-HL95010, KTIA_NAP_13-2-2015-0009 (Z.V.) and Z.V. is Bolyai Fellowship awardee.

References

1. Silva JN, Silva JR. Updates on the inherited cardiac ion channelopathies: From cell to clinical. Curr Treat Options Cardiovasc Med. 2012; 14:473–489. [PubMed: 22865245]
2. Zaydman MA, Silva JR, Cui J. Ion channel associated diseases: Overview of molecular mechanisms. Chem Rev. 2012; 112:6319–6333. [PubMed: 23151230]
3. Sheets MF, Fozzard HA, Lipkind GM, Hanck DA. Sodium channel molecular conformations and antiarrhythmic drug affinity. Trends Cardiovasc Med. 2010; 20:16–21. [PubMed: 20685573]
4. West JW, Patton DE, Scheuer T, Wang Y, Goldin AL, Catterall WA. A cluster of hydrophobic amino acid residues required for fast na(+)-channel inactivation. Proc Natl Acad Sci U S A. 1992; 89:10910–10914. [PubMed: 1332060]
5. Motoike HK, Liu H, Glaaser IW, Yang AS, Tateyama M, Kass RS. The na+ channel inactivation gate is a molecular complex: A novel role of the cooh-terminal domain. J Gen Physiol. 2004; 123:155–165. [PubMed: 14744988]
6. Silva JR, Goldstein SA. Voltage-sensor movements describe slow inactivation of voltage-gated sodium channels ii: A periodic paralysis mutation in na(v)1.4 (l689i). J Gen Physiol. 2013; 141:323–334. [PubMed: 23401572]
7. Silva JR, Goldstein SA. Voltage-sensor movements describe slow inactivation of voltage-gated sodium channels i: Wild-type skeletal muscle na(v)1.4. J Gen Physiol. 2013; 141:309–321. [PubMed: 23401571]
8. Cha A, Ruben PC, George AL Jr, Fujimoto E, Bezanilla F. Voltage sensors in domains iii and iv, but not i and ii, are immobilized by na+ channel fast inactivation. Neuron. 1999; 22:73–87. [PubMed: 10027291]
9. Chanda B, Bezanilla F. Tracking voltage-dependent conformational changes in skeletal muscle sodium channel during activation. J Gen Physiol. 2002; 120:629–645. [PubMed: 12407076]
10. Capes DL, Goldschen-Ohm MP, Arcisio-Miranda M, Bezanilla F, Chanda B. Domain iv voltage-sensor movement is both sufficient and rate limiting for fast inactivation in sodium channels. J Gen Physiol. 2013; 142:101–112. [PubMed: 23858005]
11. Campos FV, Chanda B, Beirao PS, Bezanilla F. Beta-scorpion toxin modifies gating transitions in all four voltage sensors of the sodium channel. J Gen Physiol. 2007; 130:257–268. [PubMed: 17698594]
12. Campos FV, Chanda B, Beirao PS, Bezanilla F. Alpha-scorpion toxin impairs a conformational change that leads to fast inactivation of muscle sodium channels. J Gen Physiol. 2008; 132:251–263. [PubMed: 18663133]

13. Capes DL, Arcisio-Miranda M, Jarecki BW, French RJ, Chanda B. Gating transitions in the selectivity filter region of a sodium channel are coupled to the domain iv voltage sensor. Proc Natl Acad Sci U S A. 2012; 109:2648–2653. [PubMed: 22308389]
14. Arcisio-Miranda M, Muroi Y, Chowdhury S, Chanda B. Molecular mechanism of allosteric modification of voltage-dependent sodium channels by local anesthetics. J Gen Physiol. 2010; 136:541–554. [PubMed: 20937693]
15. Muroi Y, Chanda B. Local anesthetics disrupt energetic coupling between the voltage-sensing segments of a sodium channel. J Gen Physiol. 2009; 133:1–15. [PubMed: 19088384]
16. Vatta M, Dumaine R, Varghese G, Richard TA, Shimizu W, Aihara N, Nademanee K, Brugada R, Brugada J, Veerakul G, Li H, Bowles NE, Brugada P, Antzelevitch C, Towbin JA. Genetic and biophysical basis of sudden unexplained nocturnal death syndrome (sunds), a disease allelic to brugada syndrome. Hum Mol Genet. 2002; 11:337–345. [PubMed: 11823453]
17. Hoogendijk MG, Potse M, Linnenbank AC, Verkerk AO, den Ruijter HM, van Amersfoorth SC, Klaver EC, Beekman L, Bezzina CR, Postema PG, Tan HL, Reimer AG, van der Wal AC, Ten Harkel AD, Dalinghaus M, Vinet A, Wilde AA, de Bakker JM, Coronel R. Mechanism of right precordial st-segment elevation in structural heart disease: Excitation failure by current-to-load mismatch. Heart Rhythm. 2010; 7:238–248. [PubMed: 20022821]
18. Potet F, Mabo P, Le Coq G, Probst V, Schott JJ, Airaud F, Guihard G, Daubert JC, Escande D, Le Marec H. Novel brugada scn5a mutation leading to st segment elevation in the inferior or the right precordial leads. J Cardiovasc Electrophysiol. 2003; 14:200–203. [PubMed: 12693506]
19. Rudokas MW, Varga Z, Schubert AR, Asaro AB, Silva JR. The xenopus oocyte cut-open vaseline gap voltage-clamp technique with fluorometry. J Vis Exp. 2014 Mar 11.(85)10.3791/51040
20. Stefani E, Bezanilla F. Cut-open oocyte voltage-clamp technique. Methods Enzymol. 1998; 293:300–318. [PubMed: 9711615]
21. van Bemmelen MX, Rougier JS, Gavillet B, Apotheloz F, Daidie D, Tateyama M, Rivolta I, Thomas MA, Kass RS, Staub O, Abriel H. Cardiac voltage-gated sodium channel nav1.5 is regulated by nedd4-2 mediated ubiquitination. Circ Res. 2004; 95:284–291. [PubMed: 15217910]
22. Satin J, Kyle JW, Chen M, Bell P, Cribbs LL, Fozzard HA, Rogart RB. A mutant of ttx-resistant cardiac sodium channels with ttx-sensitive properties. Science. 1992; 256:1202–1205. [PubMed: 1375397]
23. Chen HM, Ahsan SS, Santiago-Berrios MB, Abruña HD, Webb WW. Mechanisms of quenching of alexafluorophores by natural amino acids. J Am Chem Soc. 2010; 132:7244–7245. [PubMed: 20446733]
24. Pantazis A, Savalli N, Sigg D, Neely A, Olcese R. Functional heterogeneity of the four voltage sensors of a human l-type calcium channel. Proc Natl Acad Sci U S A. 2014; 111:18381–18386. [PubMed: 25489110]
25. Chanda B, Asamoah OK, Bezanilla F. Coupling interactions between voltage sensors of the sodium channel as revealed by site-specific measurements. J Gen Physiol. 2004; 123:217–230. [PubMed: 14981134]
26. Armstrong CM, Bezanilla F. Inactivation of the sodium channel. Ii. Gating current experiments. J Gen Physiol. 1977; 70:567–590. [PubMed: 591912]
27. Sheets MF, Hanck DA. Charge immobilization of the voltage sensor in domain iv is independent of sodium current inactivation. J Physiol. 2005; 563:83–93. [PubMed: 15576449]
28. Sheets MF, Chen T, Hanck DA. Outward stabilization of the voltage sensor in domain ii but not domain i speeds inactivation of voltage-gated sodium channels. Am J Physiol Heart Circ Physiol. 2013; 305:H1213–1221. [PubMed: 23893162]
29. Sheets MF, Hanck DA. Outward stabilization of the s4 segments in domains iii and iv enhances lidocaine block of sodium channels. J Physiol. 2007; 582:317–334. [PubMed: 17510181]

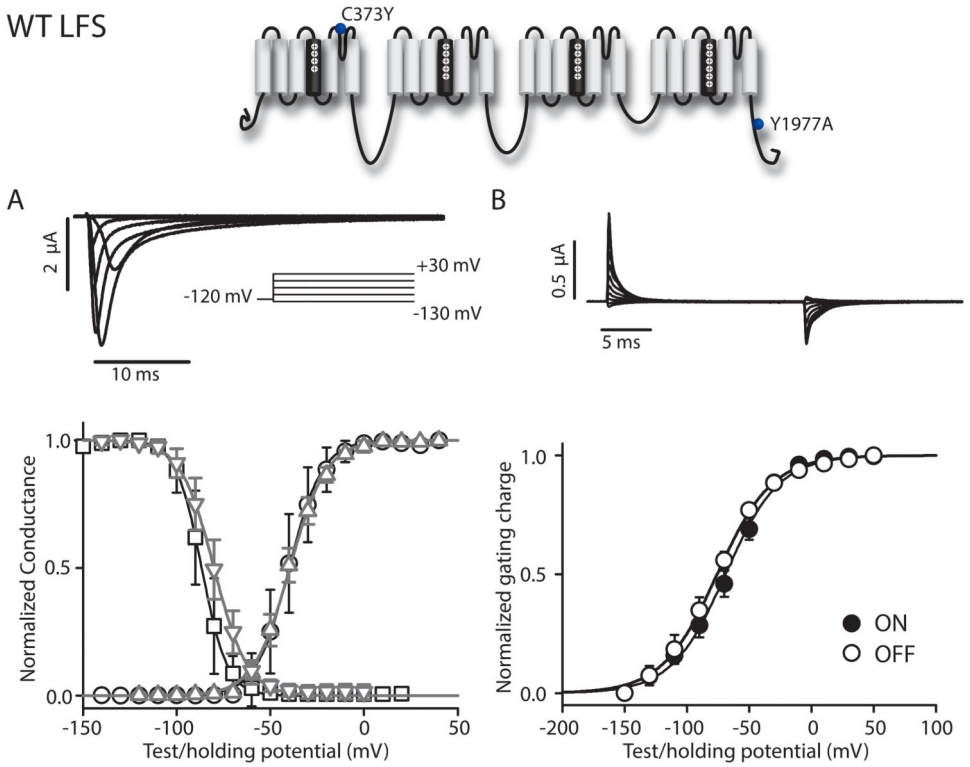

Figure 1.

WT-LFS ionic and gating currents. Currents from WT-LFS and WT channels were recorded in the cut-open oocyte configuration. The mean±95CI for groups of 6 to 22 cells are reported. (A) Top: Ionic currents. From -100 mV, a 50 ms step to -120 preceded 100 ms depolarizing pulses from -140 to +40 mV in 10 mV steps, which were followed by a 50 ms step to -120 mV before returning to holding potential. Membrane capacitance and leak were removed using P/-8 leak subtraction. For clarity, only the first 40 ms of traces corresponding to -130 to +30 mV in 20 mV steps are shown. Bottom: Voltage-dependence of steady-state activation and steady-state inactivation curves for the WT-LFS (G-V: black circles, SSI: black squares) and the WT channels (G-V, gray up triangle; SSI, gray down triangle). G-V curves were constructed from I-V relationships recorded from cells depolarized in 10 or 20 mV increments from -120 mV. Na^+ reversal potential was determined for each cell individually. For the SSI curve, cells were held at potentials ranging from -150 to +20 mV for 200 ms, and the available fraction was assessed by a -20 mV test pulse. See Table 1 for Boltzmann-fit parameters.(B) Top: Gating currents from WT-LFS channels were recorded during 20-ms depolarizing steps ranging from -150 to +50 mV in 20-mV steps. Capacitance and leak were removed using P/4 leak subtraction with a sub-sweep holding level of +40 mV. Bottom: Gating currents were integrated for 10 ms following the voltage change.

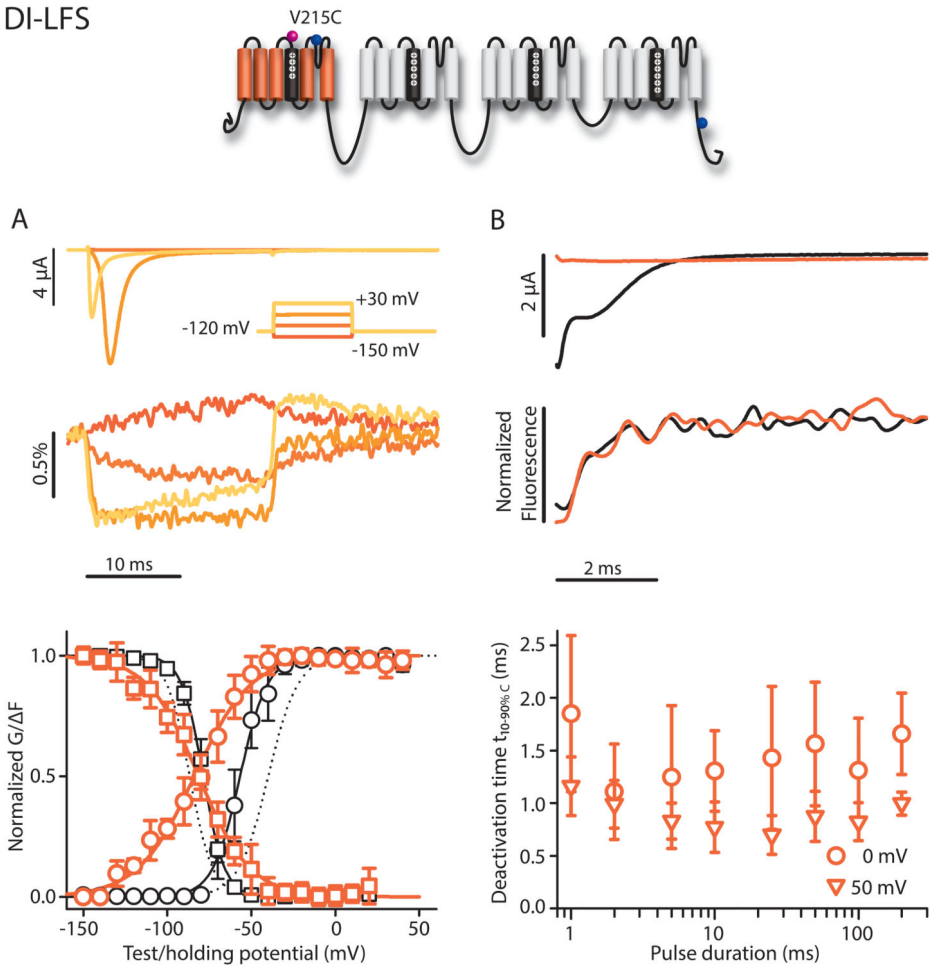

Figure 2.

V215C (DI-LFS) ionic currents and fluorescence. Na^+ currents and fluorescence were recorded from human $Na_V1.5$ channels carrying the LFS-S215C mutations with cut-open oocyte voltage-clamp fluorometry, see Materials and Methods. The mean±95CI for groups of 4 to 14 cells is reported. A) Top: Ionic currents (above) and fluorescence signals (below). From -100 mV, a 50 ms step to -120 preceded 20 ms-long depolarizing pulses ranging from -150 to +30 mV in 20 mV steps. These steps were then followed by a 50 ms step to -120 mV before returning to the holding potential. Membrane capacitance and leak were removed using P/-8 leak subtraction. For clarity, only traces corresponding to -150, -90, -30, and +30 mV are shown. Bottom: G-V curve (black circles) and SSI (black squares) and the corresponding fluorescence signals (orange circles and squares, respectively). All curves were obtained by Fig. 1 protocols. The fluorescence amplitude for the FV and SSI-FV curves was determined by taking the mean of the signal for at least 3 ms at the greatest displacement of the signal. For the SSI-FV curve, ΔF was calculated as the difference between the signal amplitude measured at the conditioning potential and -20 mV. Boltzmann-fit parameters in Table 1. Dotted lines represent WT-LFS G-V and SSI curves for comparison. B) Top: Tail currents and fluorescence measured at -120 mV following depolarizing steps to +50 mV for 2 (black) or 200 ms (orange). Inactivation does not occur during the shorter pulse resulting in a large tail current. Bottom: $t_{10\text{-}90\%,C}$ values calculated

from deactivation time constants of the fluorescence signal from exponential fits following the step back to -120 mV, from depolarizing steps to 0 or +50 mV for 1 to 200 ms durations.

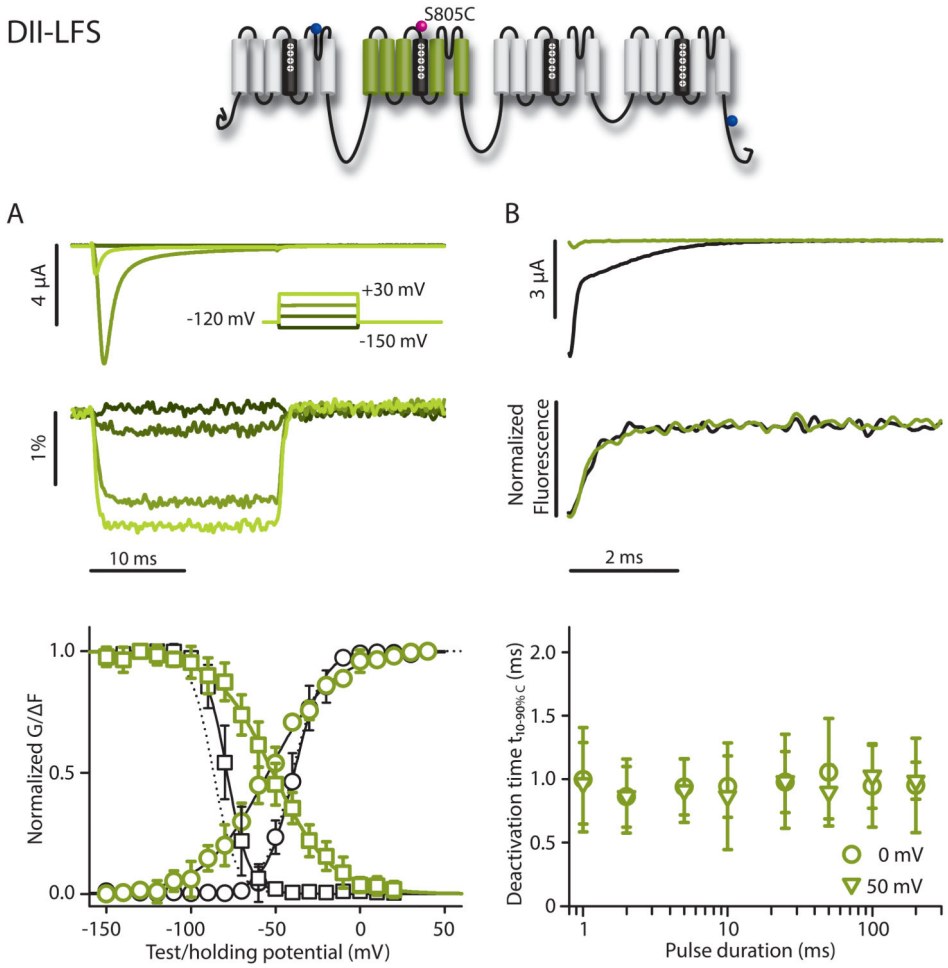

Figure 3.

DII-LFS (S805C) ionic currents and fluorescence. Na^+ currents and fluorescence were recorded from DII-LFS. Conditions were as in Figure 2 unless noted. Mean±95CI is reported for groups of 3 to 9 cells. A) Top: Ionic currents (above) and fluorescence (below). Bottom: G-V curve (black circles), SSI (black squares), and the corresponding fluorescence (green circles and squares, respectively). Curves were constructed as in Figure 2. Boltzmann-fit parameters in Table 1. Dotted lines represent WT G-V and SSI curves for comparison. B) Tail currents and fluorescence measured following the step back to -120 mV from depolarizing steps to +50 mV for 2 (black) or 200 ms (green). $t_{10\text{-}90\%,C}$ values calculated from deactivation time constants of the fluorescence signal from exponential fits following the step back to -120 mV, from depolarizing steps to 0 or +50 mV for 1 to 200 ms durations.

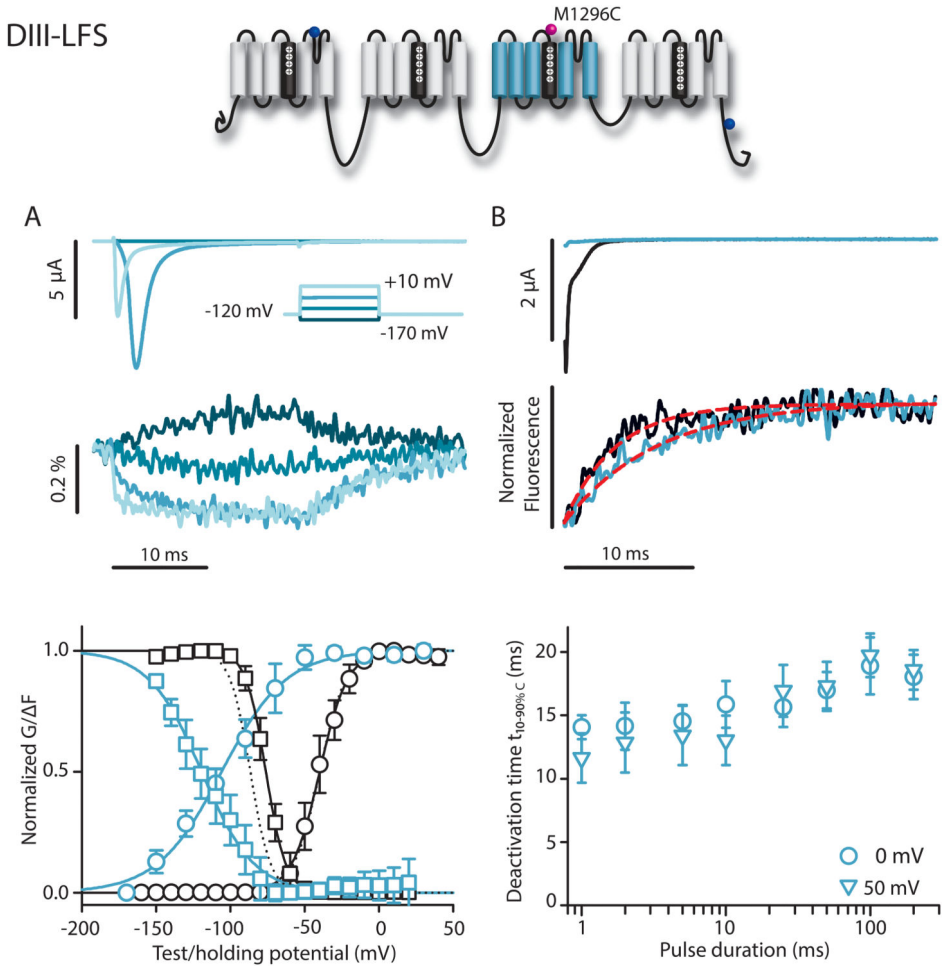

Figure 4.

DIII-LFS (M1296C) ionic currents and fluorescence. Na^+ currents and fluorescence from DIII-LFS. Mean±95CI is reported for groups of 5 to 17 cells. A) Top: Ionic currents (above) and fluorescence (below) were recorded during 20 ms pulses ranging from -170 to +30 mV in 20 mV steps. For clarity, only traces corresponding to -170, -110, -50, and +10 mV are shown. Bottom: G-V (black circles), SSI (black squares), and the corresponding fluorescence signals (blue circles and squares, respectively). Curves were constructed as in Figure 2. Boltzmann-fit parameters in Table 1. For comparison, dotted lines represent WT G-V and SSI curves. B) Tail currents and fluorescence measured following the step back to -120 mV from depolarizing steps to +50 mV for 2 (black) or 200 ms (green) pulses. Red dotted lines indicate exponential fits to the fluorescence traces. Time constants for this cell were 4.1 and 7.5 ms after 2 and 200 ms-long depolarizations, respectively. $t_{10\text{-}90\%,C}$ values calculated from deactivation time constants of the fluorescence signal from exponential fits following the step back to -120 mV, from depolarizing steps to 0 or +50 mV for 1 to 200 ms durations.

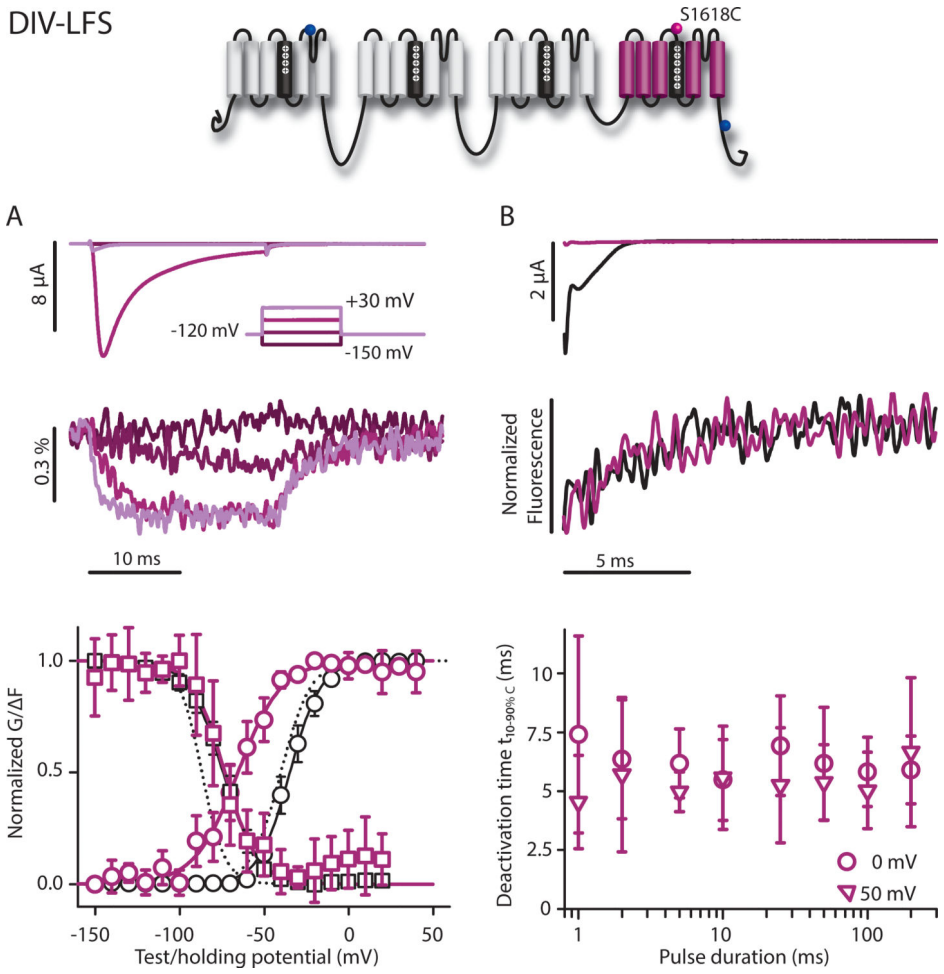

Figure 5.

DIV-LFS (S1618C) ionic currents and fluorescence. Na^+ currents and fluorescence from DIV-LFS. Mean±95CI is reported for groups of 3 to 20 cells. A) Top: Ionic currents (above) and fluorescence (below) as in Figure 2. Only traces from -150, -90, -30, and +30 mV are shown for clarity. G-V (black circles) and SSI (black squares), and the corresponding fluorescence signals (purple circles and squares, respectively). Curves were constructed as in Figure 2. Boltzmann-fit parameters in Table 1. Dotted lines represent WT G-V and SSI curves for comparison. B) Top: Tail currents and fluorescence measured during step back to -120 mV from steps to +50 mV for 2 (black) or 200 ms (green) pulses. Bottom: $t_{10\text{-}90\%,C}$ values calculated from deactivation time constants of the fluorescence signal from exponential fits following the step back to -120 mV, from depolarizing steps to 0 or +50 mV for 1 to 200 ms durations.

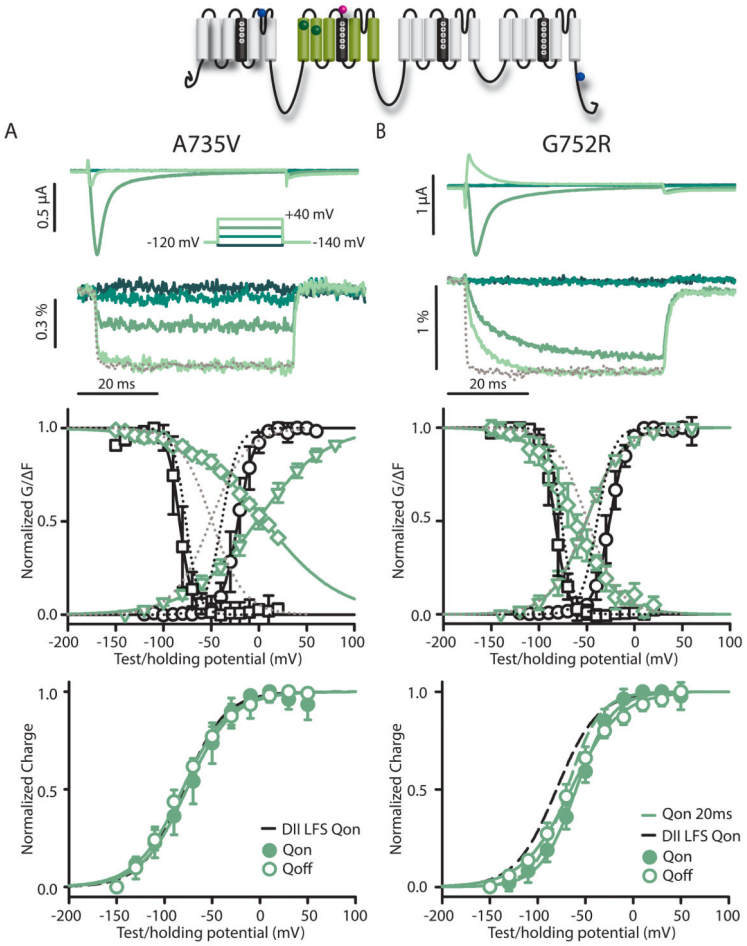

Figure 6.

DII-LFS-A735V and DII-LFS-G752R Brugada syndrome mutants. Na^+ currents and fluorescence were recorded from A735V (left panels) and G752R (right panels) mutations in the DII-LFS background. Mean±95CI is reported for groups of 3 to 8 cells. Ionic currents (top) and fluorescence (below) from DII-LFS-A735V (A) and DII-LFS-G752R (B) channels were recorded during 50 ms-long pulses ranging from -140 to +60 mV in 20 mV steps. For clarity, only -140, -80, -20 and +40 mV traces are shown. Kinetics of VSD activation in DII-LFS-A735V and DII-LFS-G752R channels are tracked by the fluorescence signal. For comparison the gray dotted line represents a normalized signal from DII-LFS recorded at +40 mV. G-V (black circles) and SSI (black squares), and the corresponding fluorescence signals (green circles and squares, respectively) for DII-LFS-A735V and DII-LFS-G752R channels. For comparison, dotted lines represent DII-LFS curves. Voltage-dependence of integrated gating charge movement over 10 ms for A735V and G752R channels. Dashed black line indicates the Q-V function of the ON gating current of WT-LFS for reference. For G752R, dashed green line shows gating charge calculated from a 20 ms interval.

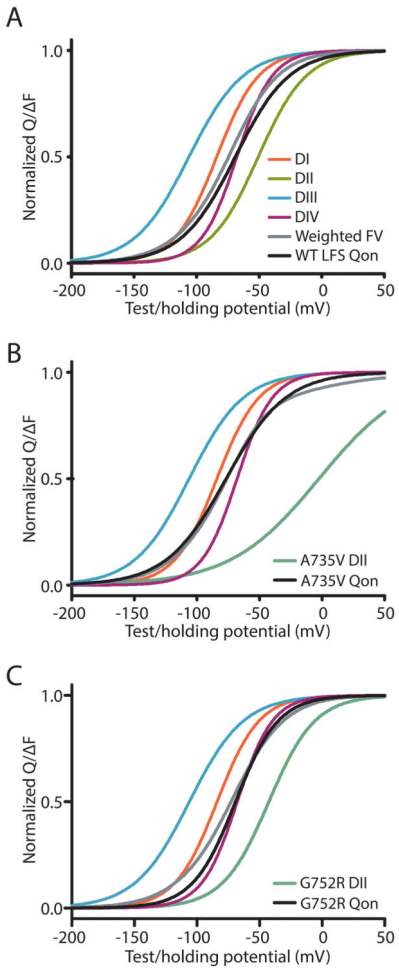

Figure 7.

Comparison of valence-weighted F-V functions to Q-V functions. F-V curves from each domain and the valence-weighted sum of these functions[24] (grey) are shown along with the Q-V curves (black) for (A) WT-LFS, (B) A735V and (C) G752R. For G752R, the 20 ms integral is shown (Fig 6B), and the F-V was also measured at 20 ms.

Table 1

Parameters of Boltzmann-fits to G-V, F-V, SSI, SSI-FV and Q-V curves

		WT	WT-LFS	DI-LFS	DII-LFS	DIII-LFS	DIV-LFS	A735V	G752R
G-V	$V_{1/2}$	-39.6±2.5	-39.9±7.1	-56.7±5.0	-38.9±3.0	-40.0±4.4	-34.6±3.4	-21.8±6.2	-25.9±3.7
	k n	9.7±1.0 (20)	8.8±1.2 (7)	8.2±1.5 (13)	8.5±1.2 (9)	9.4±0.7 (13)	9.2±0.6 (19)	8.6±1.1 (5)	8.7±0.7 (7)
SSI	$V_{1/2}$	-80.6±6.0	-86.6±5.7	-78.6±2.1	-79.2±4.5	-76.2±2.5	-74.2±3.1	-83.1±6.5	-83.2±3.9
	k n	-8.4±0.8 (22)	-6.8±0.5 (6)	-6.4±0.2 (8)	-6.5±0.9 (7)	-6.7±0.4 (17)	-10.3±0.9 (13)	-6.6±0.4 (3)	-6.8±0.8 (6)
F-V	$V_{1/2}$			-83.9±6.9	-51.4±6.7	-106.0±7.6	-66.8±8.3	-2.3±7.8	-50.4±3.3
	k n			16.8±2.9 (7)	20.5±2.3 (8)	21.7±2.1 (8)	14.6±2.9 (12)	35.4±1.7 (5)	18.7±2.6 (8)
SSIF-V	$V_{1/2}$			-81.4±5.3	-52.2±6.7	-119.4±7.2	-75.0±8.0	6.0±5.2	-62.0±5.6
	k n			-15.4±1.9 (5)	-17.5±1.7 (6)	-17.7±1.7 (5)	-10.9±4.5 (4)	-39.5±5.6 (3)	-21.5±3.2 (7)
Q_{ON}	$V_{1/2}$		-69.1±4.2	-77.8±16.5	-80.0±7.6	-71.6±2.9	-66.6±8.7	-75.6±8.3	-58.5±4.9
	k n		21.4±2.0 (7)	24.8±2.9 (4)	21.6±3.5 (4)	25.6±1.0 (5)	27.1±2.7 (5)	23.6±1.9 (5)	19.6±3.6 (6)
Q_{OFF}	$V_{1/2}$		-75.8±3.9	-74.9±7.3	-75.8±4.1	-71.2±10.9	-66.8±8.6	-79.7±3.3	-65.0±5.1
	k n		22.1±2.7 (7)	25.5±6.0 (4)	22.6±4.5 (4)	28.6±4.2 (5)	23.9±5.6 (5)	25.3±4.2 (5)	25.2±3.1 (6)

Errors represent 95% confidence intervals, numbers in parentheses indicate the number of cells measured